Nanoscale

Accepted Manuscript

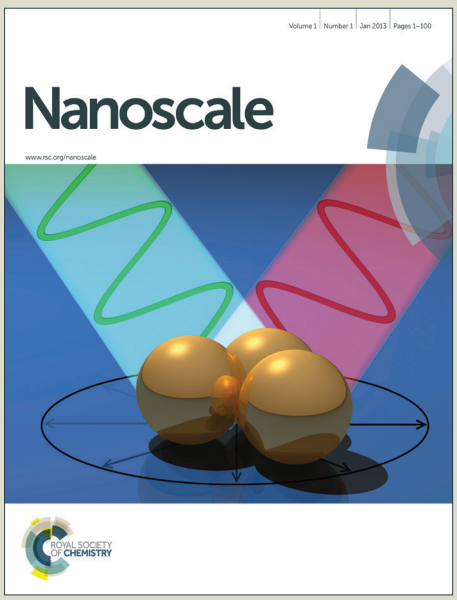

ROYAL SOCIETY OF CHEMISTRY

www.rsc.org/nanoscale

Intriguing Transmission Electron Microscopic Images Observed for Perpendicularly-Oriented Cylindrical Microdomains of Block Copolymers

Hiroshi Ohnogi[1], Toshiyuki Isshiki[2], Sono Sasaki[1], Shinichi Sakurai[1,*]

[1]Department of Biobased Materials Science, Graduate School of Science and Technology, Kyoto Institute of Technology, Matsugasaki, Sakyo-ku, Kyoto 606-8585, Japan

[2]Department of Electronics, Graduate School of Science and Technology, Kyoto Institute of Technology, Matsugasaki, Sakyo-ku, Kyoto 606-8585, Japan, isshiki@kit.ac.jp

* To whom correspondence should be addressed. (shin@kit.ac.jp)

Key Word: grain / moiré / transmission electron microscope / block copolymers / cylinder / microdomains / hexagonal lattice

Abstract

Intriguing images of dislocation structures were observed by the transmission electron microscopic (TEM) technique for hexagonally packed cylindrical microdomains in a block copolymer (polystyrene-*block*-polyethylenebutylene-*block*-polystyrene triblock copolymer) film. The polystyrene (PS) cylinders are embedded in the polyethylenebutylene (PEB) matrix and they are oriented perpendicular to the surface of the thin section for the TEM observation. In order to understand such strange dislocation structures, we applied the image processing technique with the two-dimensional Fourier transform (FT) and the inverse Fourier transform (IFT) methods. It was found that those intriguing images were not ascribed to real dislocation structures but were the fake ones due to the moiré effect caused by overlapping of the hexagons with slightly mismatched orientation. Furthermore, grain boundaries in the ultrathin section can be identified by the image processing with FT and IFT methods.

Introduction

Block copolymer microdomains can be used as templates for nano-patterning [1-7]. Exclusively, perpendicularly-oriented cylinders [1,8-22] would be very useful. Not only high degree of perpendicular orientation but also long lateral order of hexagonal packing of the cylinders are required for technological application. The latter concerns a "grain" in which the cylinders pack in a uniform hexagonal lattice. Generally speaking, a block copolymer material contains many grains so that such situation is referred to as "polygrain". It is therefore important to evaluate the size of grain in the material. Studies on grains and grain boundaries are more advanced for low molecular-weight crystalline materials such as a graphene or a graphite. Transmission electron microscopy (TEM) [23], scanning tunneling microscopy (STM) [24-27], wide-angle X-ray diffraction (WAXD or XRD) [28] are widely used experimental tools for the characterization of grain. As for the block copolymer grains, not only TEM [29], but also atomic force microscopy (AFM) [30] and small-angle X-ray scattering (SAXS) [31], which respectively correspond to the STM and WAXD techniques, have been utilized. Additionally, characteristic techniques such as the polarized optical microscopy (POM) [32,33] and the depolarized light scattering (Hv-SALS) [34] have been applied exclusively to cylindrical microdomain systems. These exclusive techniques are enabled by the use of the optical feature of cylindrical microdomains, which is the form birefringence, the refractive indices parallel and perpendicular to the cylinder axis are different so that birefringence feature is imparted when viewed from the direction perpendicular to the cylinder axis [20].

Among those, the TEM technique is popular. However, the TEM observation sometime provides strange images which may mislead conclusion of the microdomain structures. We have applied the image processing technique with the Fourier transform (FT) and the inverse Fourier transform (IFT) methods to understand the strange TEM images of the perpendicularly-

oriented cylinders (such strange dislocation structures are frequently observed for cylinders in general) and have successfully isolated the grains. For this purpose, the image processing freeware ImageJ, which can be obtained by downloading from the NIH website [35] was used. The primitive method we present herewith may provide people, who are not familiar with the image processing technique, with opportunity of analyzing defect or dislocation in such a regularly ordered system as a crystal [36-38] or a block copolymer microphase separation [7]. In turn, the image analysis method grades up and imparts advantage to the TEM technique, discriminating it from the other structural analyses such as AFM or SAXS, because the direct observation of grains and grain boundary and characterization of them are only available by the TEM technique. In some sense, TEM with the proper use of the image analysis method becomes comparable to a technique for analyzing nano-structures in three dimension.

Experimental

The sample used is an SEBS triblock copolymer with $M_n = 6.6 \times 10^4$, $M_w/M_n = 1.03$ (M_n: number-average molecular weight, M_w: weight-average molecular weight), total volume fraction of PS at the both ends of a block chain is 0.16, volume fraction of butylene moiety in the PEB block chain is 0.41. A selective solvent, *n*-heptane, was used for the solution casting, where *n*-heptane is good for PEB and poor for PS. To enhance solubility, methylene chloride, which is an inversely selective solvent (good for PS while very poor for PEB) was used as a co-solvent, such that the 1:1 mixture of *n*-heptane/methylene chloride was actually used. Since the methylene chloride is volatile at room temperature, it evaporates rapidly from the 5% solution of the SEBS sample. After complete evaporation of methylene chloride, *n*-heptane still remains in the solution. In this way, *n*-heptane solution of the SEBS sample was finally obtained. Complete evaporation of *n*-heptane from the solution took several days at room temperature [20]. The as-cast film with 0.5 mm thickness was further subjected to thermal annealing at 210°C for 3 hours.

The annealed sample was cryo-microtomed at 183 K using a Reichert-Jung Ultracut T with a cryo-sectioning system (Reichert-Nissei FC-S) with a diamond knife parallel to the surface of the sample so as to observe the TEM images of the cross-section of the cylinders which are perpendicularly oriented to it. One of ultra-thin sections with a thickness of ca 80 nm was placed on 400-mesh copper grids and exposed to ruthenium tetraoxide (RuO_4) vapour to stain selectively PS microdomains. TEM observation was performed at 75 kV on a H-600 instrument (HITACHI Co., Ltd). The PS microdomains were stained with RuO_4 so that they appear to be dark in the TEM micrographs, while the PEB matrix unstained appear to be bright. For the purpose of the image processing, ImageJ was used. Refer to its official website [35] for the details of ImageJ.

Results and Discussion

Figures 1a and 1b show TEM images of cylindrical micrdomains of SEBS16 oriented perpendicular to the film sample. Here, PS cylinders order in a hexagonal lattice in the PEB matrix. In Figure 1a, the ideally hexagonal pattern is identified. On the other hand, some strange patterns which reflect dislocation were found Figure 1b. In the region I of Figure 1b, a hexagonal array composed of approximately several tens of cylinders is inside of an irregular-hexagon of which perimeters are composed of several dark stripes. Such hexagonal compartments exist adjacently as a cluster. A pattern similar to one observed in the region I is seen in the region II. However, the numbers of cylinders (7 or 12 pieces) are included in each compartment, while 3 and 4 cylinders per compartment is also identified in the region III. On the other hand, in the region IV, a hexagonal array of white circles in the black background is observed, which is opposite to the situation of PS cylinders existing in the PEB matrix.

Figures 2a and 2b show the two-dimensional (2D) FT power spectra of the TEM images shown in Figures 1a and 1b, respectively. The 2D image analysis was performed on the basis of the following formulation of the discrete FT by using free software ImageJ.

$$F(q_k, q_l) = \sum_{m=1}^{M}\sum_{n=1}^{N} f(x_m, x_n)\exp(-iq_k x_m)\exp(-iq_l x_n) \qquad (1)$$

Here, $F(q_k, q_l)$ is the Fourier transform of $f(x_m, x_n)$, which is the pixel value at the Cartesian coordinate of (x_m, x_n) for $1 \le m \le M$ and $1 \le n \le N$ in the TEM micrograph, with q_k and q_l. The q_k $(1 \le k \le K)$ and q_l $(1 \le l \le L)$ are the coordinates in the Fourier space, given by

$$q_k = \frac{2\pi}{\Delta x}\frac{k}{M} \qquad (2)$$

$$q_l = \frac{2\pi}{\Delta x}\frac{l}{N} \qquad (3)$$

where Δx denotes the increment of x_m and x_n, namely $\Delta x = x_{m+1} - x_m = x_{n+1} - x_n$. Then, the power spectra are calculated by $F(q_k, q_l) \cdot F^*(q_k, q_l)$, where $F^*(q_k, q_l)$ denotes the complex conjugate of $F(q_k, q_l)$. A six-fold pattern is obtained as shown in Figure 2a corresponding to an almost regular-hexagonal array in Figure 1a. However, a complicated FT pattern where 3 sets of 6 spots are identified as so-called first-order peaks closest to the origin of the 2D-FT image in Figure 2b. Those are sorted out into 3 sets as shown with open circles, cross, and x-markers in the inset of Figure 2b. Since one set of 6 spots corresponds to hexagonal regions whose lattice orientation is the same, the fact that 3 sets of 6 spots are found in Figure 2b suggests existence of three hexagonal regions having different lattice orientation in the original TEM micrograph (Figure 1b). We hereafter refer to such an area where hexagonal lattice dimension and orientation are uniform as a grain. Note here that Figures 2a and 2b show deformed hexagonal patterns. The reason why perfect hexagons were not observed may be attributed to the possibility that microtoming happened to deform the samples in which a perfect hexagonal array

of cylinders is even formed. Another possibility is that the sample might be sliced not perpendicularly to the cylinder axes.

We will now perform IFT of the FT image shown in Figure 2b. In order to extract features of the original TEM image (Figure 1b), one set of six spots of the first-order peaks were chosen with a mask having six apertures. Here, we employed the round-shaped aperture. When the aperture size is small enough to encircle each peak, a hexagonal array with long-range order can be visualized in an obtained IFT image. Since lattice distortion (disorder of the second kind) may exist in a real grain, the smallest aperture size results in over-estimation of the grain size. On the other hand, when the aperture size is too big, unfavorable information coming from neighboring spots is mixed so that a part of neighboring grain will appear additionally in the IFT image. In order to introduce a criterion for determination of the aperture size, one dimensional profile of a first-order FT peak is examined. Figure 3 shows the circularly averaged pixel values plotted as a function of the pixel position from the center of the selected spot with an arrow in the inset of Figure 2b. The solid curve shown in Figure 3 is a fitted one with the Gaussian function on the basis of the least-squares method. As seen here, the 1D profile of the first-order peak can be expressed by the Gauss function so that the aperture radius was set to the half-width at the half-maximum of the Gaussian peak. For this particular case, the aperture radius was determined to 5 pixels, corresponding to the aperture area of 97 pixels (total number of pixels existing inside of the circle with the diameter of 10 pixels and those including the arc of the circle of which occupation per pixel is 50% and above).

Figure 4 shows gray-scale IFT images (constructed according to the gradation scale bar from 0 to 20 pixel value shown in the figure) of Figure 2b, which are obtained from the limited area of the FT image around six spot 1st-order peaks (3 sets as shown in the inset of Figure 2b with markers x, +, and o), each of the 3 sets being extracted by using masks illustrated in the insets of Figures 4a, 4b, and 4c, respectively, where the aperture area is 97 pixels around each of the six

spots and the aperture area of 1 pixel at the origin of the FT image. Note that the value of the masked pixel was reset to 0 before conducting IFT by using also ImageJ. Formulation of the discrete IFT is given by

$$f(x_m, x_n) = \frac{1}{K}\frac{1}{L}\sum_k\sum_l F(q_k, q_l)\exp(iq_k x_m)\exp(iq_l x_n) \qquad (4)$$

A region of the hexagonal array is retrieved in each of Figures 4a, 4b, and 4c. However, it is very difficult to identify a singe grain of the hexagonal array in these gray-scale images because contrast of the hexagonal array decreases monotonically with the distance from the center of the grain. Note that this feature is characteristic of IFT from a masked FT image. Therefore, binarization of the gray-scale images is required in order to specify the grain in the IFT image. As a matter of fact, the binarized image appears differently depending on the value of threshold. Therefore, it should be optimized. Figure 5 shows the binarized IFT images with the most optimal threshold value which is 1. Other binarized images with different threshold values are presented in Supplementary Information for the aperture size of 97 pixels to examine effects of threshold.

Figure 5a is obtained as black-and-white images from the gray-scale IFT images shown in Figure 4a by resetting pixel values to 0 (black) for the case of the original pixel value lower than the threshold value and resetting them to 255 (white) for the other case. Similarly, those shown in Figures 5b and 5c were converted from the gray-scale IFT images shown in Figures 4b and 4c, which were respectively obtained by filtering another set of the representative 6 spots of the 1st-order peaks in the FT image as shown in the inset of Figure 2b with crosses and open circles, respectively. It is shown in the Supplementary Information that the region of the hexagonal array becomes larger for the larger threshold value in the black-and-white images because the pixel having a value lower than the threshold value becomes dark. Furthermore, there is a

region in Figures 5a and 5b where cylinders are merged with each other in one direction. Since such a region should be eliminated by the image analysis, this means that our method is not perfect.

Here, the criterion for optimization of the threshold value is explained. The optimal threshold is so determined as the most of characteristic features in the original TEM image in Figure 1b (as specified with regions I, II, III, and IV) can be reproduced by superimposing three IFT images shown in Figures 5a, 5b, and 5c. Actually, comparing the original TEM image with the superimposed ones shown in Figure 8, where not only the image binarized with the optimal value of the threshold but also others with the threshold values of 2, 3, and 4 are exhibited for comparison, it is clearly seen that images shown in the panels (c) and (d) in Figure 6 overestimate the regions II and III of Figure 1b. Therefore, the threshold values 1 and 2 are the candidates for the appropriate one. However it is impossible to distinguish the difference between two images as shown in the panels (a) and (b) in Figure 6. Since the smaller value is better, the threshold value of 1 was so selected (Figure 6a), although the feature specified with the region I in Figure 1b was unfortunately not reproduced in Figure 6a. This method of optimization of the threshold value by trial-and-error is primitive so that an advanced method is anticipated.

It can be recognized that a peculiar pattern appears in the region where two binarized IFT images overlap, which is created by the moiré effect, not the real dislocation. As a matter of fact, Luchnikov et. al. [7] have experimentally shown that the moiré patterns appeared in the TEM micrograph when two pieces of nanoporous thin films were superimposed, where the nanopores with ca. 13 nm of diameter were pierced with the hexagonal array in the thin films. Especially, quite similar images to ours, which appear in the regions I and III in Figure 1b, were observed. Generally speaking, a coarse hexagonal pattern appears by the moiré effect, so that people may have impression that those peculiar patterns are far from the common sense of the moiré pattern. However, it can be understood that the magnified moiré pattern looks

dislocation. To demonstrate this point, some examples of overlapped images are shown in Figure 7, where a couple of identical hexagonal arrays of black circles are overlapped with a misorientation angle ϕ in parts (a)-(c), which are similar to the characteristic features observed in the original TEM image of Figure 1b as specified with regions I, II, and III, respectively (so-called the rotation moiré, which is quantified in detail by Luchnikov et. al. [7]). Figure 7d is an exception, which is resulted by superimposing the images with parallel shift of a quarter phase (without twisting). This reproduces the characteristic features observed in the region IV in Figure 1b.

We are now in the position of demonstrating application of the FT-IFT image analysis to structural analyses of grain. Figure 8a shows the TEM micrograph (the same as that shown in Figure 1b) with three curves indicating grain boundaries, which are determined by the FT-IFT image analysis. Thus-determined grains are found to be overlapped. The distance 542 nm shown in the figure indicates a typical overlapping distance. To understand the three-dimensional situation of the grains, the schematic illustration for the grain boundary (inclined to the thin section) in the ultrathin section of the sample for the TEM observation is shown in Figure 8b. In this figure, θ is an oblique angle of the grain boundary with respect to the thin section of the sample. Since the thickness of the sample section is ca 80 nm, the oblique angle can be calculated as,

$$\theta = \tan^{-1}\left(\frac{80}{542}\right) \approx 8.4^{\circ} \qquad (5)$$

which is very small. This means the grain boundary is almost parallel to the thin section. Note here that two grains contain perpendicularly oriented cylinders with different hexagonal lattice. Namely, although cylinder orientation is identical, the cylinders are subjected to disconnect at the grain boundary, as depicted schematically in Figure 9. Further inspection of the three-

dimensional structure at the grain boundary is required to understand how the mismatched cylinders merge together at the grain boundary.

Conclusions

We applied the image processing technique on the basis of the FT and IFT methods to analyze grain boundary structures observed in the TEM micrograph exhibiting peculiar moiré patterns, which comprises grains of perpendicularly-oriented cylinders having slightly different orientation of the hexagonal lattice. For this purpose, we used the image processing freeware ImageJ, which can be obtained by downloading from the NIH website without charge. Therefore, the primitive method we reported herewith may provide people, who are not familiar with the image processing technique, with opportunity of analyzing defect or dislocation in such a regularly ordered system as a crystal or a block copolymer microphase separation. We eventually ascribed the region, where such peculiar moiré pattern appears, to the inclined grain boundary happened to be accommodated by chance in the thin section for the TEM observation.

References

1 P. Mansky, C. K. Harrison, P. M. Chaikin, R. A. Register and N. Yao, *Appl. Phys. Lett.*, 1996, **68**, 2586-2588.

2 M. Park, C. Harrison, P. M. Chaikin, R. A. Register and D. H. Adamson, *Science*, 1997, **276**, 1401-1404.

3 C. De Rosa, C. Park, E. L. Thomas and B. Lotz, *Nature*, 2000, **405**, 433-437.

4 M. Park, P. M. Chaikin, R. A. Register and D. H. Adamson, *Appl. Phys. Lett.*, 2001, **79**, 257-259.

5 C, Harrison, J. A. Dagata and D. H. Adamson, in *Developments in Block Copolymer Science and Technology*, ed. I. W. Hamley, John Wiley & Sons, Chichester, England, 2004, ch 9, pp 295-323

6 H. Kitano, S. Akasaka, T. Inoue, F. Chen, M. Takenaka, H. Hasegawa, H. Yoshida and H. Nagano, *Langmuir*, 2007, **23**, 6404-6410.

7 V. Luchnikov, A. Kondyurin, P. Formanek, H. Lichte and M. Stamm, *Nano Lett*., 2007, **7**, 3628-3632.

8 A. Turturro, E. Gattiglia, P. Vacca and G. T. Viola, *Polymer*, 1995, **36**, 3987-3996.

9 P. Mansky, P. Chaikin and E. L. Thomas, *J. Mater. Sci*., 1995, **30**, 1987-1992.

10 T. L. Morkved, M. Lu, A. M. Urbas, E. E. Ehrichs, H. M. Jaeger, P. Mansky and T. P. Russell, *Science*, 1996, **273**, 931-933.

11 G. Kim and M. Libera, *Macromolecules*, 1998, **31**, 2569-2577.

12 T. Thurn-Albrecht, J. Schotter, G. A. Kästle, N. Emley, T. Shibauchi, L. Krusin-Elbaum, K. Guarini, C. T. Black, M. T. Tuominen, and T. P. Russell, *Science*, 2000, **290**, 2126-2129.

13 Z.Q. Lin, D.H. Kim, X.D. Wu, L. Boosahda, D. Stone, L. LaRose and T.P. Russell, *Adv. Mater.*, 2002, **14**, 1373-1376.

14 K. Shin, K. A. Leach, J. T. Goldbach, D. H. Kim, J. Y. Jho, M. Tuominen, C. J. Hawker and T. P. Russell, *Nano Lett.*, 2002, **2**, 933–936.

15 E. Sivaniah, Y. Hayashi, M. lino, T. Hashimoto and K. Fukunaga, *Macromolecules*, 2003, **36**, 5894-5896; E. Sivaniah, Y. Hayashi, S. Matsubara, S. Kiyono, T. Hashimoto, K. Fukunaga, E.J. Kramer and T. Mates, *Macromolecules*, 2005, **38**, 1837-1849.

16 S.H. Kim, M.J. Misner, T. Xu , M. Kimura and T.P. Russell, *Adv. Mater.*, 2004, **16**, 226-231.

17 S. Sakurai, S. Okamoto and K. Sakurai, in *Developments in Block Copolymer Science and Technology*, ed. I. W. Hamley, John Wiley & Sons, Chichester, England, 2004, ch 4, pp 127-158.

18 R. M. Ho, W. H. Tseng, H. W. Fan, Y. W. Chiang, C. C. Lin, B. T. Ko and B. H. Huang, *Polymer*, 2005, **46**, 9362-9377.

19 (a) K. Watanabe, H. Yoshida, K. Kamata and T. Iyoda, *Trans. Mater. Res. Soc. Jpn.*, 2005, **30**, 377-381. (b) Y. Morikawa, S. Nagano, K. Watanabe, K. Kamata, T. Iyoda and T. Seki, *Adv. Mater*., 2006, **18**, 883-886.

20 S. Sakurai, H. Bando, H. Yoshida, R. Fukuoka, M. Mouri, K. Yamamoto and S. Okamoto, *Macromolecules*, 2009, **42**, 2115–2121.

21 T. Matsutani and K. Yamamoto, *J. Phys.: Conf. Ser.*, 2011, **272**, 012015.

22 G. Cui, M. Fujikawa, S. Nagano, T. Miyazaki, S. Sakurai and K. Yamamoto, *Nanoscale*, 2013, **5**, 6713-6719.

23 Y. Shi, W. Zhou, A. Y. Lu, W. Fang, Y. H. Lee, A. L. Hsu, S. M. Kim, K. K. Kim, H. Y. Yang, L. J. Li, J. C. Idrobo, and J. Kong, *Nano Lett.*, 2012, **12**, 2784–2791.

24 P. Simonis, C. Goffaux, P. A. Thiry, L. P. Biro, Ph. Lambin, and V. Meunier, *Surf. Sci*., 2002, **511**, 319–322.

25 J. Coraux, A. T. N'Diaye, C. Busse, and T. Michely, *Nano Lett*., 2008, **8**, 565–570.

26 L. B. Biedermann, M. L. Bolen, M. A. Capano, D. Zemlyanov, and R. G. Reifenberger, *Phys. Rev. B*, 2009, **79**, 125411.

27 J. Cervenka and C. F. J. Flipse, *Phys. Rev. B*, 2009, **79**, 195429.

28 K. Kim, Z. Lee, W. Regan, C. Kisielowski, M. F. Crommie, and A. Zettl, *ACS Nano*, 2011, **5**, 2142–2146.

29 S. Koizumi, H. Hasegawa, and T. Hashimoto, *Macromolecules*, 1994, **27**, 6532-6540.

30 K. G. Yager, N. J. Fredin, X. Zhang, B. C. Berry, A. Karim and R. L. Jones, *Soft Matter*, 2010, **6**, 92-99.

31 S. Okamoto, S. Ito, K. Ando, M. Mouri, A. Ikeda, H. Hasegawa, and N. Koshikawa, *IOP Conf.Ser. Mater. Sci. Eng*., 2010, **14**, 014008.

32 K. Kimishima, T. Koga, and T. Hashimoto, *Macromolecules*, 2000, **33**, 968-977.

33 T. Q. Chastek and T. P. Lodge, *Macromolecules*, 2004, **37**, 4891-4899.

34 H. Yamanishi, H. Ohnogi, S. Sakurai, to be submitted (2014).

35 W.S. Rasband, ImageJ, U. S. National Institutes of Health, Bethesda, Maryland, USA, http://imagej.nih.gov/ij/, 1997-2014.

36 T. Isshiki, M. Ohta, K. Nishio and M. Shiojiri, *Thin Solid Films*, 1995, **271**, 84-87.

37 J. Reyes-Gasga, S. Tehuacanero and M. José Yacamán, *Microsc. Res. Tech*., 1998, **40**, 2-9.

38 L.P. Ferroni, G. Pezzotti, T. Isshiki and H.-J. Kleebe, *Acta Mater*., 2001, **49**, 2109-2113.

Figure Caption

Figure 1 Transmission eleectron microscopic (TEM) images of perpendicularly oriented cylinders of the SEBS triblock copolymers. The polystyrene (PS) microphase was stained with RuO_4 so that it appears dark in the TEM images. The PS cylinders are

embedded in the unstained poly(ethylenebutylene) matrix and they are oriented perpendicular to the surface of the SEBS film. Panel (a) shows almost ideally hexagonal packing of the cylinders (the inset shows enlarged view) while panel (b) shows peculiar (characteristic) feature which is much different from an ideally hexagonal pattern.

Figure 2 Fourier transform (FT) images (power spectra) of TEM images shown in Figures 1. The inset of Figure 2(b) emphasizes the positions of the 1st-order peaks of the FT power spectra appearing in the image (b).

Figure 3 Example of the power spectra for one of the spots shown with the x markers in Figure 2(b), which exist in the direction of nine o'clock from the origin. The pixel values around the center of the selected spot are circularly averaged and plotted here as a function of the pixel position from the center.

Figure 4 Grayscale images of invese FT from FT image shown in Figure 2(b), which are obtained from the limited area of the FT image around six spots of the 1st-order peaks (3 sets as shown in the inset of Figure 2(b) with markers x, +, and ○), each of the 3 sets being extracted by using masks illustrated in the insets of (a), (b), and (c), respectively, where the aperture size is 97 pixels around each of the six spots and the aperture size of 1 pixel at the origin of the FT image. Note that the whole FT image was not used in this procedure.

Figure 5 Binarized images from the grayscale inverse FT images shown in Figure 4. The value of the threshold is 1 for all of the images.

Figure 6 Corresponding superimposed images from those shown in Figures 5 and S1-S3 in the Supplementary Information. The values of the threshold are 1, 2, 3, and 4 for the parts (a), (b), (c), and (d), respectively.

Figure 7 Representative moiré patterns featuring the peculiar (characteristic) patterns seen in the TEM micrograph. Those moiré patterns are obtained by superimposing a couple of the identical hexagonally-ordered circles with the misorientation angle ϕ (= 4°, 14°, and 19°) indicated in each pattern. One exception is resulted by superimposing the hexagonal patterns with parallel (horizontal) shift of a quater phase (without twisting, namely $\phi = 0°$).

Figure 8 (a) TEM micrograph showing peculiar (characteristic) patterns which are much different from the perfect hexagonal pattern. Three curves indicate grain boundaries, which are determined by the moiré analysis. Thus determined grains are found to be overlapped. The distance 734.6 nm shown in the figure indicates a typical overlapping distance. (b) Schematic illustration for the grain boundary in the ultrathin section of the sample for the TEM observation (inclined to the thin section).

Figure 9 Schematic illustration for a possible explanation of the reason why the grain boundary is inclined to the thin section for the TEM observation.

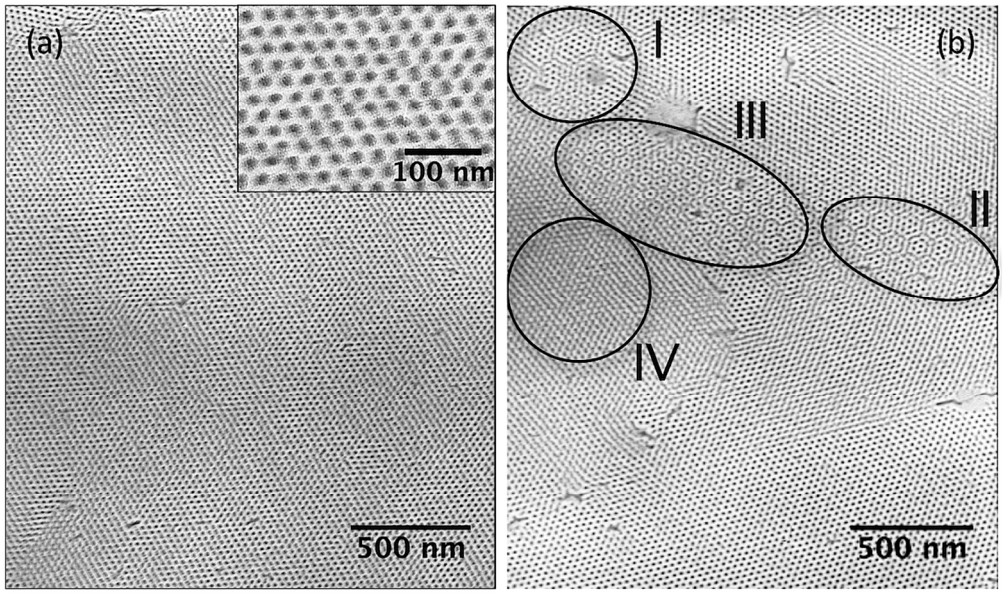

Figure 1 Transmission eleectron microscopic (TEM) images of perpendicularly oriented cylinders of the SEBS triblock copolymers. The polystyrene (PS) microphase was stained with RuO4 so that it appears dark in the TEM images. The PS cylinders are embedded in the unstained poly(ethylenebutylene) matrix and they are oriented perpendicular to the surface of the SEBS film. Panel (a) shows almost ideally hexagonal packing of the cylinders (the inset shows enlarged view) while panel (b) shows peculiar (characteristic) feature which is much different from an ideally hexagonal pattern.
170x100mm (200 x 200 DPI)

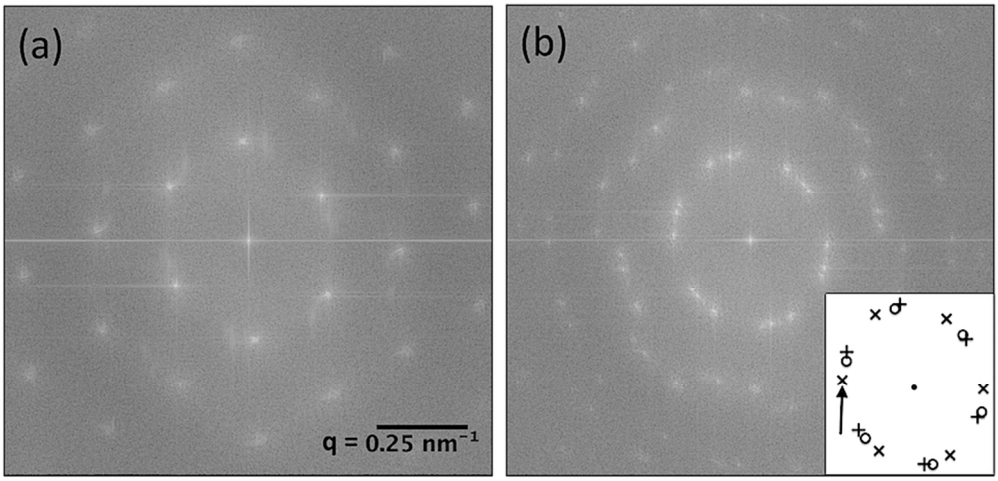

Figure 2 Fourier transform (FT) images (power spectra) of TEM images shown in Figures 1. The inset of Figure 2(b) emphasizes the positions of the 1st-order peaks of the FT power spectra appearing in the image (b).
82x39mm (300 x 300 DPI)

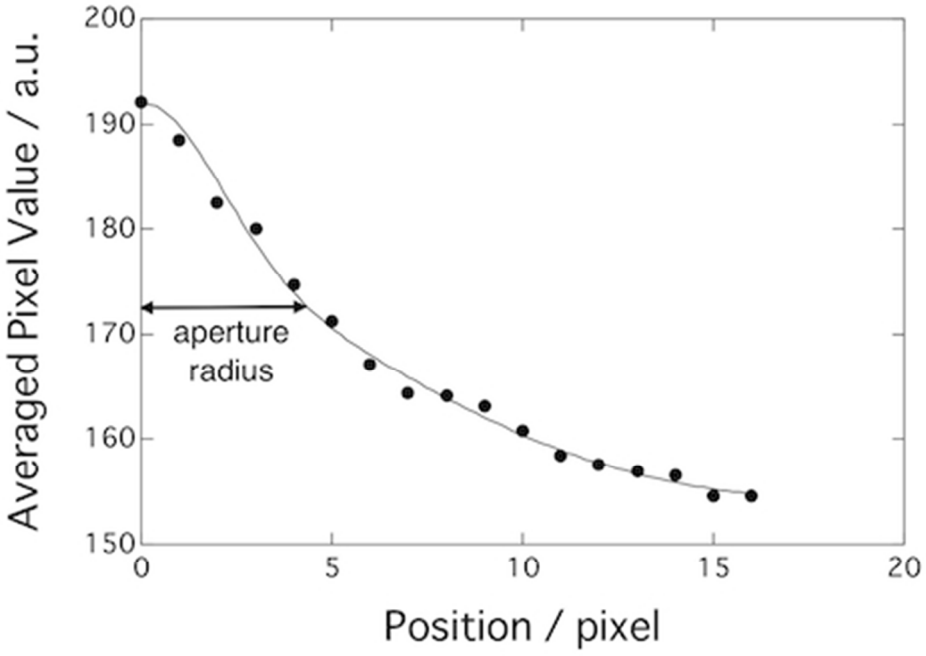

Figure 3 Example of the power spectra for one of the spots shown with the x markers in Figure 2(b), which exist in the direction of nine o'clock from the origin. The pixel values around the center of the selected spot are circularly averaged and plotted here as a function of the pixel position from the center.
82x56mm (150 x 150 DPI)

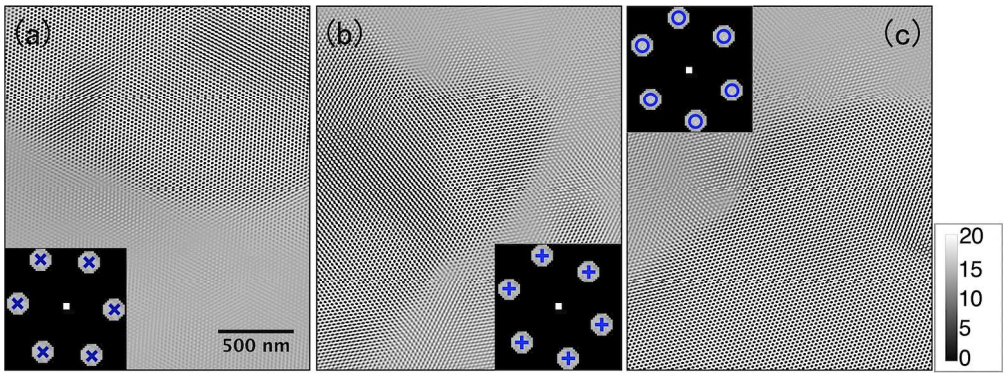

Figure 4 Grayscale images of invese FT from FT image shown in Figure 2(b), which are obtained from the limited area of the FT image around six spots of the 1st-order peaks (3 sets as shown in the inset of Figure 2(b) with markers x, +, and ○), each of the 3 sets being extracted by using masks illustrated in the insets of (a), (b), and (c), respectively, where the aperture size is 97 pixels around each of the six spots and the aperture size of 1 pixel at the origin of the FT image. Note that the whole FT image was not used in this procedure.
170x62mm (300 x 300 DPI)

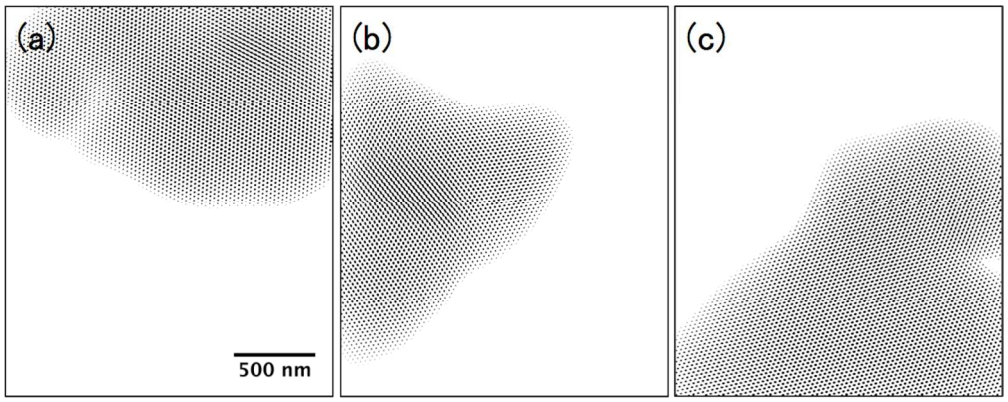

Figure 5 Binarized images from the grayscale inverse FT images shown in Figure 4. The value of the threshold is 1 for all of the images.
170x66mm (300 x 300 DPI)

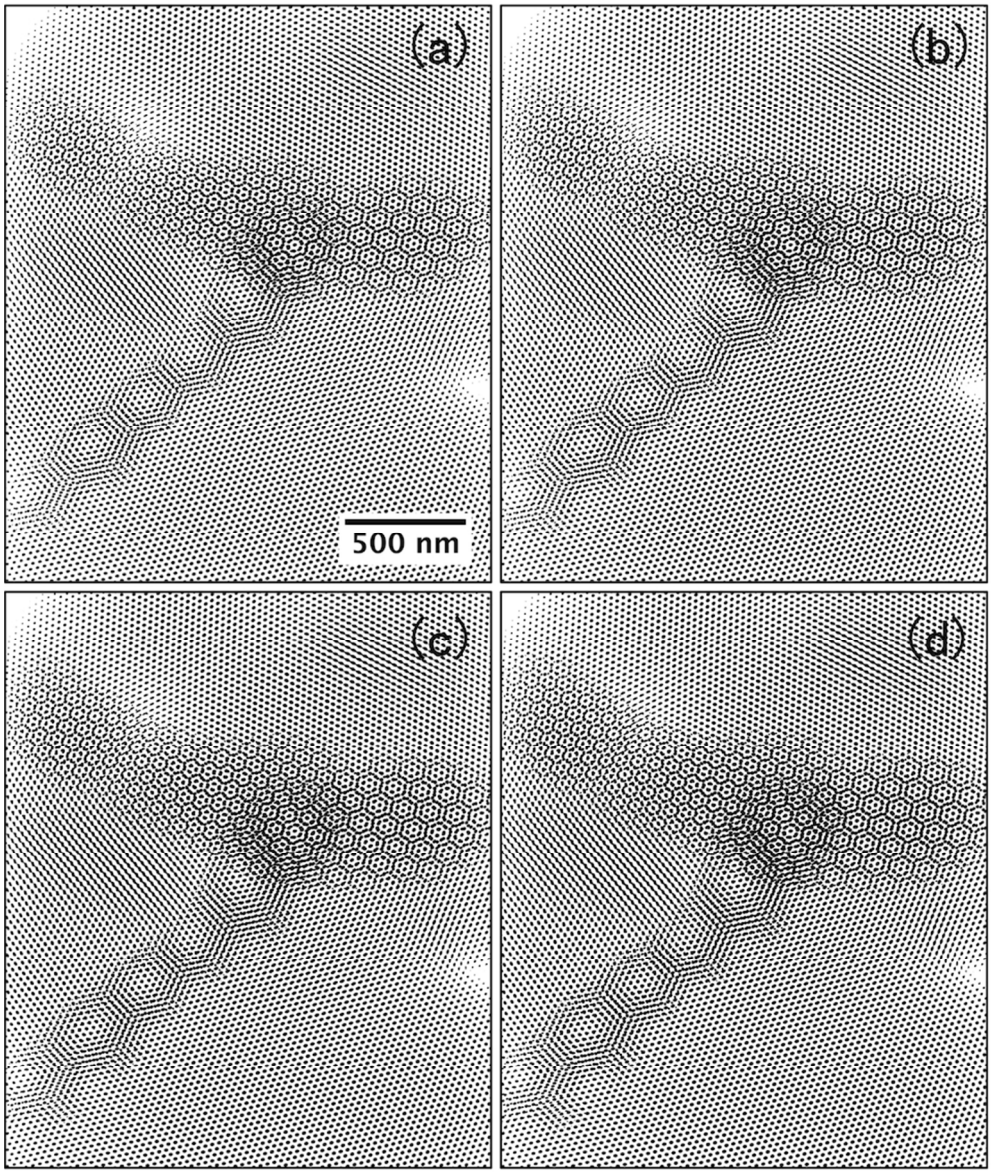

Figure 6 Corresponding superimposed images from those shown in Figures 5 and S1-S3 in the Supplementary Information. The values of the threshold are 1, 2, 3, and 4 for the parts (a), (b), (c), and (d), respectively.
82x96mm (300 x 300 DPI)

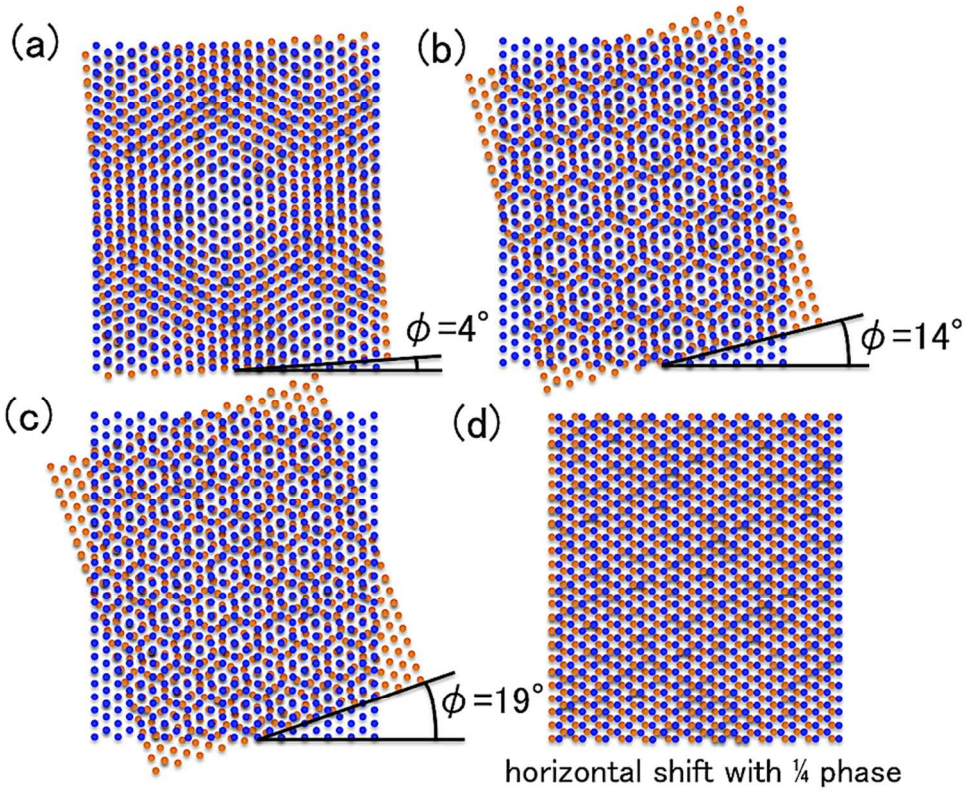

Figure 7 Representative moiré patterns featuring the peculiar (characteristic) patterns seen in the TEM micrograph. Those moiré patterns are obtained by superimposing a couple of the identical hexagonally-ordered circles with the misorientation angle φ(= 4°, 14°, and 19°) indicated in each pattern. One exception is resulted by superimposing the hexagonal patterns with parallel (horizontal) shift of a quater phase (without twisting, namelyφ= 0°).
82x65mm (300 x 300 DPI)

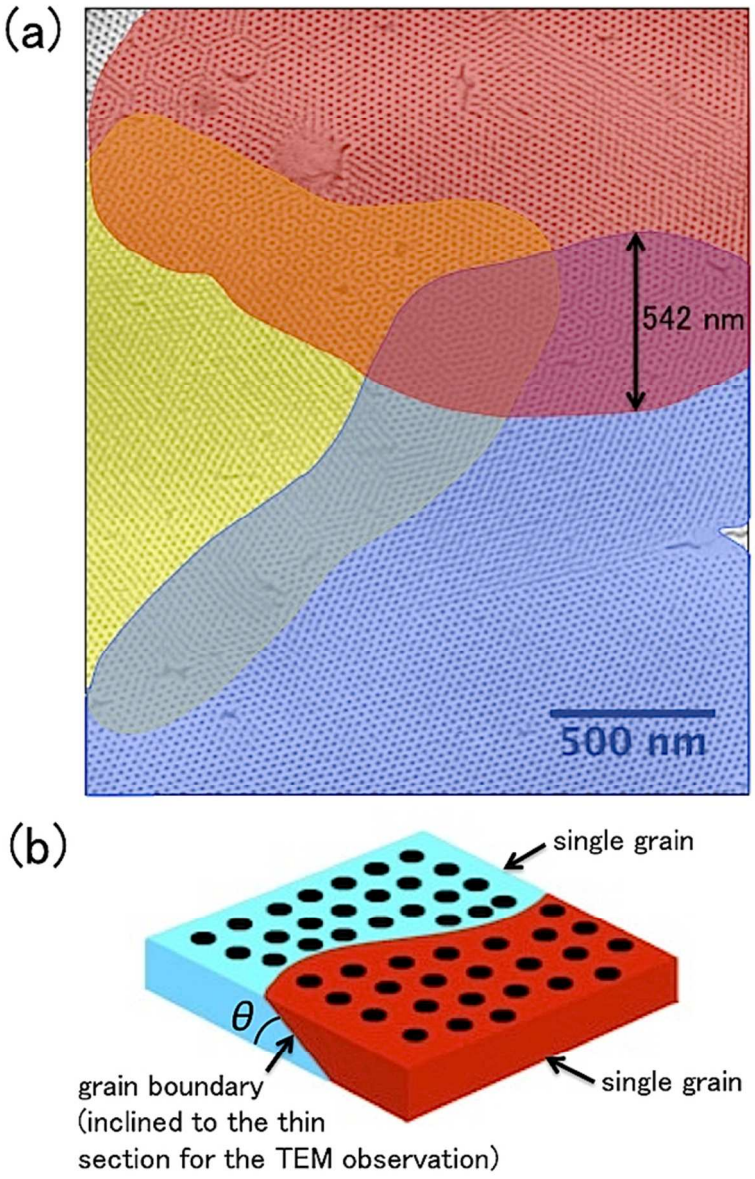

Figure 8 (a) TEM micrograph showing peculiar (characteristic) patterns which are much different from the perfect hexagonal pattern. Three curves indicate grain boundaries, which are determined by the moiré analysis. Thus determined grains are found to be overlapped. The distance 734.6 nm shown in the figure indicates a typical overlapping distance. (b) Schematic illustration for the grain boundary in the ultrathin section of the sample for the TEM observation (inclined to the thin section).
82x127mm (200 x 200 DPI)

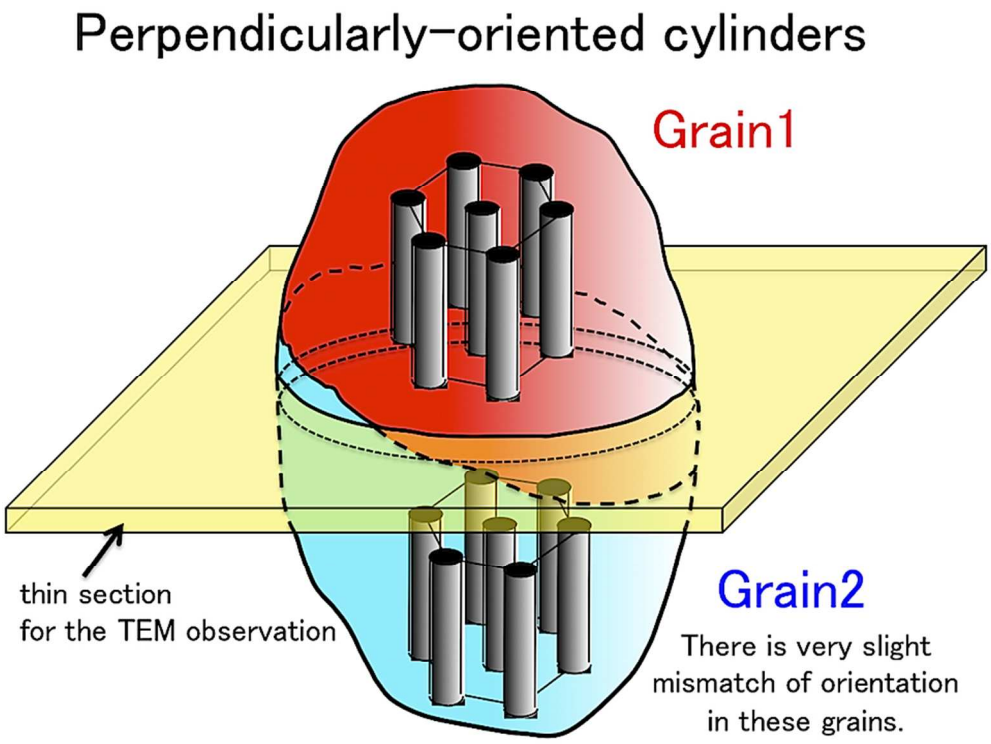

Figure 9 Schematic illustration for a possible explanation of the reason why the grain boundary is inclined to the thin section for the TEM observation.
82x62mm (300 x 300 DPI)